Linearization of a longwave radiation scheme for intermediate tropical atmospheric models

Chia Chou

Department of Atmospheric Sciences, University of California, Los Angeles

J. David Neelin

Department of Atmospheric Sciences and Institute of Geophysics and Planetary Physics,
University of California, Los Angeles

Abstract. A Green's function method is presented for linearizing longwave radiation schemes commonly used in general circulation models in order to produce simpler schemes suitable for use in intermediate complexity atmospheric models. Nonlocal dependence of radiative fluxes on vertical distributions of temperature, moisture, cloud fraction, and cloud top are retained, consistent with the nonlinear scheme. Treatment of several cloud cover types is used in linearizing cloud fraction. A weakly nonlinear scheme is also presented. The method is most useful if linearization about a single tropical reference profile has a sufficient range of validity. Tests are carried out using European Centre for Medium-Range Weather Forecasts (ECMWF) analysis fields, International Satellite Cloud Climatology Project (ISCCP), Comprehensive Ocean-Atmosphere Data Set (COADS) and outgoing longwave radiation (OLR) data, and the Harshvardhan scheme as the nonlinear scheme. The linear scheme is found to reproduce the nonlinear results with surprising accuracy in simulation of longwave radiative fluxes associated with interannual variability, seasonal variations, and even tropical climatology as a departure from its spatial average. The spatial patterns and relative magnitudes associated with various contributions are discussed to help inform and provide a target for intermediate model simulations.

1. Introduction

The study of ocean-atmosphere and atmosphere-land interaction is crucial to understanding tropical climate phenomena. Simple models of the tropical atmosphere [*Gill*, 1980; *Webster*, 1981; *Zebiak*, 1986; *Lindzen and Nigam*, 1987; *Neelin and Held*, 1987; *Seager*, 1991; *Wang and Li*, 1993] have been used for many purposes, particularly problems where obtaining wind from a given heating or sea surface temperature (SST) sufficed. Although the simple models have very different assumptions about convection, and issues regarding the relative importance of various mechanisms are not resolved [e.g., *Neelin*, 1989], their results for surface wind distribution tend to be similar. However, to resolve issues of physical mechanism and to understand problems involving radiative transfer, surface heat exchange, cloud effects, and the stability of the tropical climatology, there is a need for models intermediate between these simple models and general circulation models (GCMs). An important component of such intermediate models will be the treatment of longwave radiation.

Currently, longwave radiation is treated casually in simple models of the tropical atmosphere. Newtonian cooling is the norm, often based on a crudely modeled midlevel temperature. For cases with fixed SST, this treatment for longwave radiation is adequate because of strong loss terms from atmosphere to ocean. However, when considering the coupled ocean-atmosphere or atmosphere-land system, outgoing longwave radiation (OLR) is the only thermodynamic loss term within the tropical system, so the treatment of longwave radiation becomes crucially important. Because of strong transfers within the atmospheric column, transfers between surface and atmospheric layers, and cloudiness and moisture dependence of the fluxes, Newtonian cooling becomes increasingly hard to justify and tuning the coefficient becomes difficult. One approach has been to make Newtonian cooling coefficients depend on parameterized cloudiness [*Seager and Zebiak*, 1995]. On the other hand, the more realistic longwave radiative schemes used in GCMs are perhaps more complicated than optimal for intermediate models. They also become computationally burdensome because of integrations of absorption spectra through interaction paths. For the case of clear sky and fixed absorbers, *Curtis* [1956] and *Fels and Schwarzkopf* [1981] presented schemes that made use of precomputed matrices associated with the transmission function. There appears to be strong motivation to seek an scheme in similar spirit,

but where variation of clouds and absorbers, especially water vapor, is taken into account. At the same time, for the problem at hand, the source function may plausibly be linearized. On the basis of this, we present here a rigorous and efficient approach for capturing essential aspects of a GCM scheme in a linearized (or weakly nonlinear) scheme and then test the accuracy against the original. The linearized scheme should be well suited to intermediate atmospheric models and perhaps useful to other modelers as well.

A suitably posed nonlinear GCM radiative scheme has fluxes that change smoothly as a function of the input large-scale meteorological variables, so it can be linearized with respect to all variables that have significant effects on radiative transfer. Here we present everything in terms of a two-stream scheme, which is completely adequate for our purposes for longwave radiation, although the method can be extended, for instance, to four-stream schemes [Liou, 1974]. Because the fluxes at all vertical levels are functions of temperature, moisture, etc., at all vertical levels, the linearization is given in terms of Green's functions. For grid point discretization, these are just matrices whose rank is on the order of the number of vertical levels. The Green's functions are obtained by numerical linearization of a full GCM longwave radiation code, such as Harshvardhan et al. [1987], Morcrette [1990], Ramanathan and Downey [1986], Kiehl et al. [1987], Lacis and Oinas [1991], or Chou et al. [1991].

Here, we illustrate the process using the Harshvardhan scheme. The computational effort associated with the full longwave scheme is incurred during the linearization process. Once this is done, model runs using the linearized scheme have only small multiplications of model variables with the Green's functions matrices. Two obvious questions are (1) the accuracy of the linear scheme in typical meteorological situations and (2) whether the reference profile about which the linearization is done needs to be a function of space and season to maintain sufficient accuracy. If Green's functions would need to be stored for every model grid point and season, our approach would become cumbersome and lose part of the attraction of simplicity. We thus test here the simplest possible version of the scheme using a single reference profile, independent of space and season, for tropical applications. In section 2, we outline the formulation of the linearized scheme and briefly describe the reference state prescribed in the linearization. The Green's functions and resulting fluxes are discussed in section 3. Applications to the annual average, the seasonal cycle and an El Niño-Southern Oscillation (ENSO) case are discussed in sections 4 and 5. In discussing these cases, the aims are (1) to test the accuracy with which the linear scheme (about a single reference profile) can reproduce the nonlinear scheme's radiative response in the tropics; (2) to verify that the responses of both schemes are consistent with OLR data, and to quantify the relative sizes of various contributions that would be relevant to an intermediate model simulation of the annual average Walker

circulation and its seasonal and interannual variations; (3) to point out potential uses of the linear scheme and some technical details (such as trade-off between cloud top and cloud-type linearizations); (4) to provide targets for later intermediate modeling. Conclusions are summarized in section 6.

2. Formulation

2.1. Nonlinear Scheme

In standard two-stream schemes [Liou, 1980; Goody and Yung, 1989], longwave radiative fluxes are divided into two parts: downward fluxes, $R^\downarrow$, and upward fluxes, $R^\uparrow$, under assumptions that permit integration over upgoing and downgoing angles in order to produce a one-dimensional calculation in the vertical. It is sometimes useful to distinguish between radiation originating from the lower boundary, $R^\uparrow_{sfc}$, and upward radiation originating within the atmosphere, $R^\uparrow_{atm}$, such that $R^\uparrow = R^\uparrow_{atm} + R^\uparrow_{sfc}$.

We use the Harshvardhan longwave radiation scheme [Harshvardhan et al., 1984, 1987], a two-stream radiative scheme with no reflection or scattering, as the nonlinear scheme to be linearized. Specific characteristics of this scheme are briefly described in Appendix B, along with comments on numerical approaches that are suitable for the linear analysis.

2.2 Formulation: Weakly Nonlinear and Linear Schemes

We consider five variables that have strong effects on longwave radiation: atmospheric temperature, moisture, cloud cover, and cloud top, denoted, T, q, α and p_t, respectively, and surface temperature, T_s. Extension to other variables, such as CO_2, is straightforward. The dependence of longwave radiative fluxes in these variables is smooth, so these fluxes can be linearized about a reference state to be specified later. Cloud fraction is treated with particular attention since it is important to applications of interest [Cess and Potter, 1987; Ramanathan, 1987; Randall et al., 1989; Slingo and Slingo, 1988]. We present first a weakly nonlinear scheme that retains second-order terms associated with cloud fraction because (1) it helps clarify the special treatment of cloud cover terms (see section 2.3); (2) it would cost little to use in a model; and (3) the retained second-order terms are the largest. We then specialize to a linear case.

Let G^n_X be the Green's function associated with variable X in the presence of cloud type n, where X can be T, q, α_n, p_{tn} or T_s (with α_n and p_{tn} denoting cloud fraction and cloud top associated with cloud type n). For temperature, let $G^n_T(p, \hat{p})T'(\hat{p})$ denote the radiative flux at level p associated with perturbations at level $\hat{p}$, and likewise for moisture. Then the longwave radiative fluxes, $R^\uparrow$ or $R^\downarrow$, can be written (temporarily omitting the arrows for clarity) for the weakly nonlinear version:

$$R(p) = \quad \bar{R}(p)$$
$$+ \sum_{n=0}^{N} \alpha_n < G_T^n(p,\grave{p})T'(\grave{p}) >$$
$$+ \sum_{n=0}^{N} \alpha_n < G_q^n(p,\grave{p})q'(\grave{p}) >$$
$$+ \sum_{n=1}^{N} G_{\alpha_n}(p)\alpha_n'$$
$$+ \sum_{n=1}^{N} \alpha_n G_{p_{tn}}(p)p_{tn}'$$
$$+ \sum_{n=0}^{N} \alpha_n G_{T_s}^n(p)T_s'$$
$$+ \quad higher\ order\ terms, \tag{1}$$

where

$$G_T^n(p,\grave{p}) = \partial R(p)/\partial T(\grave{p}) \tag{2a}$$

$$G_q^n(p,\grave{p}) = \partial R(p)/\partial q(\grave{p}) \tag{2b}$$

$$G_{\alpha_n}(p) = \partial R(p)/\partial \alpha_n \tag{2c}$$

$$G_{p_{tn}}(p) = \partial R(p)/\partial p_{tn} \tag{2d}$$

$$G_{T_s}^n(p) = \partial R^{\uparrow}(p)/\partial T_s. \tag{2e}$$

Here, $\overline{(\ )}$ denotes reference state value and $(\ )'$ denotes perturbations. The vertical inner product over all levels is denoted $< AB > = \Delta p^{-1} \int_{p_0}^{p_s} A(\grave{p})B(\grave{p})d\grave{p}$, where p_s is surface pressure, p_0 is pressure of the atmospheric "top" (the highest level included in the calculation), and $\Delta p = p_s - p_0$. A discrete version of (1)–(2) is given in Appendix A. In (1), $n = 0$ represents clear sky, so α_0 is the fraction of clear sky and $p_{t_0} = 0$. The partial derivatives in (2) are evaluated about the reference state $\bar{T}$, $\bar{q}$, $\bar{T}_s$, $\bar{p}_{tn}$ for the case of $\alpha_n = 1$, and $\alpha_{m\neq n} = 0$ (except 2c, see (7) below). Note that cloud fraction is treated differently from other variables in that α_n multiplies each of Green's functions before summation over the cloud types discussed in section 2.3. For the weakly nonlinear version, α_n includes both the reference state and perturbations and is thus potentially a function of x, y, and t. The second-order terms included are $\alpha_n'T'$, $\alpha_n'q'$, $\alpha_n'p_{tn}'$, etc. While perturbations here are with respect to the reference state, for the linear case, they can be subdivided, for instance, into annual average, seasonal and interannual contributions.

In (1) perturbation quantities may be any function of space or time. The formulation can potentially be applied for reference state quantities which are a function of space and season. If reference state variables (other

than α_n) depend on longitude and latitude (x,y), then one obtains $G_T^n(x,y,p,\grave{p})$ which, if calculated at high resolution in x, y would result in storing large matrices. For instance, *Zou and Navon* [1996] perform online calculations to avoid massive storage for a Jacobian matrix similar to (2b) for a solar radiation code in a tangent linear model for the National Meteorological Center GCM. One could also compute say $G_T^n(y,p,\grave{p})$ at a few latitudes y and interpolate. Here we use the simplest case: a reference state with $\bar{T}$, $\bar{q}$, $\bar{p}_{tn}$, $\bar{T}_s$ independent of space and time, resulting in $G_T^n(p,\grave{p})$ only. The treatment of cloud types permits linearization of cloud cover terms about a reference state $\bar{\alpha}_n$ in (1) that could be a function of space and season even if the reference state in $\bar{T}$ and $\bar{q}$ is not. In that case (1) would be used with α_n replaced by $\bar{\alpha}_n$. We find that the special case with $\bar{\alpha}_n$ independent of space and season gives good results and simplifies (1) because summation over cloud types can be done without creating large matrices. This linearized case condenses to:

$$R(p) = \quad \bar{R}(p)$$
$$+ \quad < G_T(p,\grave{p})T'(\grave{p}) >$$
$$+ \quad < G_q(p,\grave{p})q'(\grave{p}) >$$
$$+ \sum_{n=1}^{N} G_{\alpha_n}(p)\alpha_n'$$
$$+ \sum_{n=1}^{N} \bar{\alpha}_n G_{p_{tn}}(p)p_{tn}'$$
$$+ \quad G_{T_s}(p)T_s' \tag{3}$$

where

$$G_X = \sum_{n=0}^{N} \bar{\alpha}_n G_X^n. \tag{4}$$

The quantity $\bar{R}$ in (3) is independent of space and season and is precomputed once using the nonlinear scheme.

For compactness and numerical efficiency, the first four Green's functions in (1) or (3) include terms due to both $R_{atm}^{\uparrow}$ and absorption of $R_{sfc}^{\uparrow}$ due to T', q', α_n', and p_{tn}'. The $G_{T_s}^n$ term contains only perturbations in $R_{sfc}^{\uparrow}$ directly due to T_s'. For interpretation and comparison with the nonlinear scheme, we also discuss the behavior of $R_{sfc}^{\uparrow}$ separately in section 3, which involves combining the $G_{T_s}^n$ term with appropriate contributions from each of the other G_X^n terms, calculated separately.

When applied in an atmospheric model, the atmospheric heating due to longwave radiation can be computed from Green's functions of the form (2) using (1) and $Q_{LW} = \partial_p R^{\uparrow} - \partial_p R^{\downarrow}$. An alternate formulation would be to use Green's functions H_X^n that directly give the heating rate. For the case corresponding to (3) this would be:

$$Q'_{LW}(p) = \quad < H_T(p,\hat{p})T'(\hat{p}) >$$
$$+ \quad < H_q(p,\hat{p})q'(\hat{p}) >$$
$$+ \quad \sum_{n=1}^{N} H_{\alpha_n}(p)\alpha'_n$$
$$+ \quad \sum_{n=1}^{N} \bar{\alpha}_n H_{p_{tn}}(p)p'_{tn}$$
$$+ \quad H_{T_s}(p)T'_s. \tag{5}$$

This is numerically more compact as discussed in Appendix A, and may be handier to use in modeling applications. The form (1)–(2) is used in presentation since it is closer to the original scheme and contains more information. The Green's functions of (5) can be derived from those of (2) by

$$H^n_X = g/C_p(\partial_p G^{n\uparrow}_X - \partial_p G^{n\downarrow}_X). \tag{6}$$

We note that for four-stream schemes or shortwave calculations it may prove easier to employ form (5), calculating H^n_X directly from the nonlinear scheme. For a clear sky case with no moisture variation, the first term in (5) is akin to the *Curtis* [1956] method, if the source function in the latter is linearized. *Fels and Schwarzkopf* [1981] use a slightly different approach that involves linearization of the transmission function with respect to temperature, for fixed absorbers, resulting in a three-index matrix which they then approximately factorize to two indices.

2.3 Cloud Cover and Cloud Type Treatment

Definition of cloud type based on satellite data is often done in terms of cloud top pressure and optical depth for shortwave radiation. *Rossow and Schiffer* [1991] suggest a seven cloud-type classification. *Ockert-Bell and Hartmann* [1992] propose a simpler classification with five cloud types. The simplest one provided in the International Satellite Cloud Climatology Project (ISCCP) data set is the classical three cloud-type (high, middle, low) classified by cloud top pressure. For longwave radiation, clouds of significant depth may be assumed black, so specification of cloud top and base is adequate. Clouds are sometimes parameterized in GCMs as filling the layers in which convection is occurring or relative humidity is high, or may depend on explicit liquid water budgets.

We have two considerations in defining cloud types: (1) the constraint that linearization must work over a large range of cloud fraction (2) to provide flexibility in the way that cloud type would be specified from intermediate atmospheric models providing different levels of detail in relevant variables. We meet these considerations by defining "cloud cover types" rather than cloud types as normally defined ("cloud type" is used often for brevity hereafter). Figure 1 provides a schematic of simple cloud cover types that might be used. A crucial trick for linearization is that we define cloud types as never overlapping in the vertical. For instance, if overlapping high cloud and low cloud (such as types 3 and 4 in Figure 1) are to be included, this must be defined as a separate cloud type (such as type 5 in Figure 1). This allows the full range of cloud fraction for each cloud type to be treated linearly, as in the formulation (1). For convenience, cloud cover types such as type 1 in Figure 1 can be constructed for dynamically related cloud combinations. For instance, the intensity of deep convection in a model can be used to parameterize the cloud fraction of the tower anvil
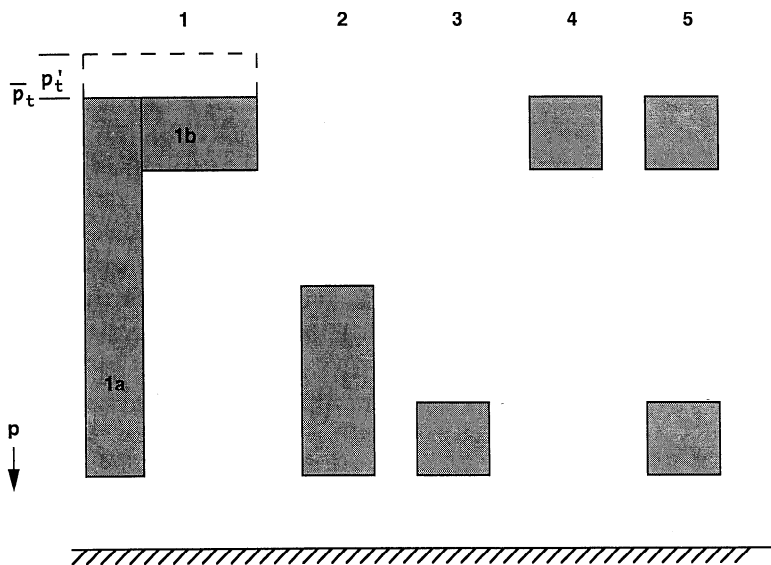

Figure 1. Schematic examples of cloud cover types. Cloud type 5 is included to illustrate the nonoverlap approach: overlap in the vertical is permitted only by defining another cloud cover type. Cloud cover type 1 illustrates a useful combination (see text). Green's functions for cloud fraction are based on fixed cloud structure, for example, mean cloud top, $\bar{p}_{tn}$ for each type. Variations of cloud top, p'_{tn}, are taken into account separately for each type.

combination type 1, even if the model does not provide enough information to separately calculate fractions for deep clouds 1a and thinner high clouds 1b. For the presentation here, we use types 1, 2, and 3 of Figure 1, since the basic ISCCP classification does not distinguish types such as 5 of Figure 1 and because *Ockert-Bell and Hartmann* [1992] point out that a three cloud-type model produces OLR similar to more complex classifications. The combination for type 1 is specified according to $G_X^1 = (\alpha_{1a}/\alpha_1)G_X^{1a} + (\alpha_{1b}/\alpha_1)G_X^{1b}$, with the relative fractions of 1a and 1b fixed. For illustration here we specify the ratio $\alpha_{1a}/\alpha_{1b} = 1/3$ from the idealized tropical cloud cluster distribution of *Houze* [1982]. We note that the distinction between 1a and 1b does not affect OLR, but does impact the vertical structure of the fluxes within the atmosphere.

The cloud cover types have fixed vertical structure when the radiative response per change in cloud fraction of a given type is computed from the nonlinear scheme. Details of cloud properties, such as transmittance and emissivity, are handled within the nonlinear scheme. It is desirable to keep only a limited number of cloud types, so there are limitations on the cloud vertical structure that can be resolved. However, important changes in cloud vertical structure within each type can be treated directly within the linearization, notably cloud top variations. As schematized in Figure 1, this permits variations in the vertical extent of each cloud type to be included, with small changes handled very accurately.

Because the dependence on cloud fraction is fully linear under this treatment, the Green's function for cloud fraction can be given relative to the clear sky case (this is why the summation over cloud types in (1) omits $\alpha = 0$). Thus (2c) becomes

$$G_{\alpha_n}(p) = R(p)|_{\alpha_n=1} - R(p)|_{\alpha_0=1} \qquad (7)$$

The Green's function for cloud top is estimated in discretized form using the nonlinear scheme with cloud top at levels $\bar{p}_t$ and $\bar{p}_t + \Delta p$, respectively, where Δp is the increment through the layer below $\bar{p}_t$. Then (2d) becomes

$$G_{p_{tn}}^{\uparrow}(p) = (R^{\uparrow}(p)|_{\bar{p}_{tn}+\Delta p} - R^{\uparrow}(p)|_{\bar{p}_{tn}})/\Delta p \qquad (8)$$

for the upward flux. The downward flux changes are immediately reabsorbed within the cloud layer, so for $p_t' < \Delta p$, it is more accurate to set $G_{p_{tn}}^{\downarrow} = 0$ than to use the equivalent of (8). We note that if $p_t' < \Delta p$, the nonlinear scheme cannot handle cloud top variations, so the linear scheme will actually be more accurate than the nonlinear scheme at coarse vertical resolution in this respect.

In summary, we are allowed to choose the vertical structures by which we represent cloudiness. We make our choice of cloud cover types differently than the conventional GCM level-by-level representation to roughly optimize the efficiency with which typical cloudiness conditions can be represented by a few cloudiness variables for linearization. For instance, defining a "deep cloud" cover type with a typical depth and variations about this depth (e.g., type 1a) captures a common condition much more effectively for present purposes than if variables representing cloud fraction at each of many levels were individually used in linearization. Obviously, there are also limitations to this method, for instance, if details of many cloud configurations become important.

2.4 Data

To test the linearized scheme against the original nonlinear version, observations are used to prescribe T, T_s, q, cloud cover α and cloud top p_t. The atmospheric temperature and moisture are from the European Center for Medium-range Weather Forecasts (ECMWF) analyses of the World Meteorological Organization (WMO). SST is from the Comprehensive Ocean-Atmosphere Data Set (COADS). SST is simply extrapolated over land areas for present purposes. The cloud cover and cloud top are from the C2 product of the International Satellite Cloud Climatology Project (ISCCP) data. The classification of cloud is associated with the classical morphological cloud types defined by cloud top pressure in the ISCCP data [*Rossow and Schiffer*, 1991]: low cloud below 680 mbar, middle cloud 440-680 mbar and high cloud above 440 mbar. OLR, which we use to compare to the results of the linearized scheme and the fully nonlinear scheme, is obtained from the Climate Analysis Center (CAC) at the National Meteorological Center. ISCCP data with average cloud cover and cloud top for a one cloud-type classification were also used for comparison.

3. Idealized Cases

Since fluxes at every level depend on moisture and temperature at every level, it is not practical nor informative to display the full Green's functions and their nonlinear counterparts. Instead we display fluxes, especially OLR, for specified perturbations. Realistic cases are considered in sections 4 and 5. Here we use idealized vertical structures of temperature and moisture perturbations to discuss the degree of nonlinearity of the flux dependence, and some details of cloud top dependence.

3.1 Temperature and Moisture Dependence (Clear Sky Case)

Since temperature perturbations are often vertically coherent, a reasonable test profile is $T'(\dot{p}) = $ constant; we also add an SST perturbation T_s' having the same value. The normalized error between fluxes from the nonlinear scheme, $R'(p)$ and from the linear scheme, $(R'(p) - < G_T^0(p, \dot{p})T'(\dot{p}) >)/R'(p)$ is used as a diagnostic of the range of validity of the linear scheme. Figure 2 shows the error for selected flux components. For a 5°K temperature increase of the column, the linearized scheme underestimates the perturbation by less than 5%. Thus only modest errors occur over a range of temperature perturbations that is substantial for the tropical troposphere. We note that the temperature dependence for fluxes arising within the atmosphere
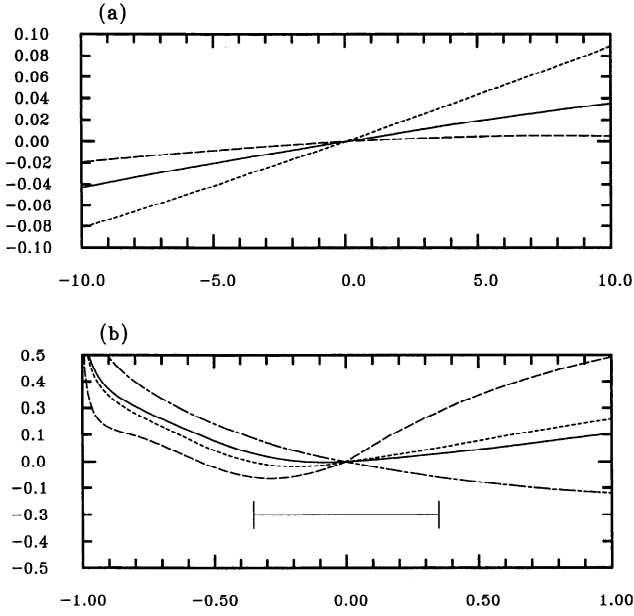
Figure 2. (a) Normalized error $(R' - G_T^0 T')/R'$ versus T' for selected flux components: $R^{\downarrow}$ at the surface (solid line); $R_{atm}^{\uparrow}$ at the top of the atmosphere (dashed line); and $R_{sfc}^{\uparrow}$ at the top of the atmosphere (dotted line). T' is the same at each model layer as well as the surface. (b) Normalized error $(R' - G_q^0 q')/R'$ versus q' for the same flux components as Figure 2a plus total OLR (dot-dashed line). The specified moisture perturbation is given in the text. The moisture perturbation values on the abscissa are scaled such that 1 represents the whole atmospheric column being saturated, and -1 represents no water vapor in the column. The line at the bottom of Figure 2b roughly indicates the range within which two thirds of the tropical area is located in these coordinates.

is even more linear than would be expected from the Stefan-Boltzmann σT^4 emission dependence. This is because contributions from the second derivative of the Planck function and second derivative of the transmittance tend to cancel (see *Liou* [1980], equation (4.79) and (4.80); errors are associated with the second derivative of the flux). This range of validity is sufficiently large that we can use a single reference temperature profile in the tropics, for instance, a time-space mean over the tropics. Thus we apply a Green's function, $G_T^n(p, \hat{p})$ that is not a function of x and y, to all tropical areas.

The linearization of moisture dependence is more worrisome because moisture varies through a large range, comparable to the tropical mean value at each level. Figure 2b shows the normalized error $(R'(p) - < G_q^0(p, \hat{p})$ $q'(\hat{p}) >)/R'(p)$ for selected fluxes as a function of specific humidity perturbation, q'. Because supersaturated or negative values of moisture would render the calculation meaningless if we simply specified a vertical structure and considered large positive and negative perturbations, we specify the moisture perturbations from the reference profile as follows. For positive per-

turbations, we take the moisture perturbation to be a given fraction of the difference between $\bar{q}$ and the local saturation value, $q_{sat}(\bar{T})$, at each level. For negative perturbations, we likewise specify fractions of the difference between $\bar{q}$ and zero at each level. We thus consider perturbations over the range from a completely dry column ($q' = -1$ in this coordinate) to completely saturated ($q' = 1$). The differences between fluxes from the nonlinear and the linear schemes can reach more than 30 % for $R_{atm}^{\uparrow}$ when the column is completely dry or saturated. Fortunately, for most areas of interest, the error is smaller. Most of the tropics lies in a much smaller range. To give an idea of this for the annual average climatology, we indicate the range in which two thirds of tropical points (30N—30S) may be found, in terms of total column water vapor content. The worst component fractional error is almost 15% for $R_{atm}^{\uparrow}$ for $q' = 0.35$. However, when combined with $R_{sfc}^{\uparrow}$ to give total OLR (dot-dashed curve), the latter dominates, and furthermore, errors in the two components tend to cancel. The resulting OLR error is only about 5% for $q' = 0.35$.

3.2 Dependence on Mean Cloud Top

When considering cloudy regions, it is useful to have a quantitative feel for how upward fluxes, particularly OLR, depend on mean cloud top, given "typical" perturbations in T', T_s', q', α_n' and p_{tn}'. The physics associated with each Green's function is mentioned briefly for orientation, although the processes are familiar from greenhouse effect summaries [e.g., *Houghton et al.*, 1990]. Here a cloud that fills the interval between 950 mbar and $\bar{p}_{tn}$ is considered, with $\bar{p}_{tn}$ running through values that would normally be divided into several cloud types. Figure 3 shows the OLR associated with $G_X^n X'$ for perturbations of reasonable magnitude (and vertical structure) for each quantity. Figure 3a shows the relationship between $(< G_T^n(p = 0, \hat{p}) T' > + G_{T_s}^n (p = 0) T_s')$ and $\bar{p}_{tn}$ with $T'(p) = 1K$ for all p and $T_s' = 1K$. The OLR perturbations range from 4 Wm^{-2} for $\bar{p}_{tn} = 900$ mbar to 0.5 Wm^{-2} for $\bar{p}_{tn} = 100$ mbar. The OLR decreases monotonically as cloud top becomes higher, even though T' is constant, because $\sigma \bar{T}^3$ gets smaller at cloud top and fluxes from below are absorbed. For the case of a positive moisture perturbation (Figure 3b) the OLR perturbation is negative since the dominant effect is the water vapor greenhouse effect increasing absorption of fluxes from below. Increasing cloud top effectively varies the level of emission so there is a smaller flux being absorbed by the water vapor perturbation, and also the column water vapor above cloud top is smaller. For the case of a positive cloud fraction perturbation (Figure 3c) the OLR is likewise negative due to increased absorption. High clouds have a much stronger contribution than lower clouds since they absorb and reemit from a lower temperature. For typical magnitudes of the perturbations, this term has a stronger effect than the others. In Figure 3d, a positive cloud top perturbation, p_{tn}', increases OLR because
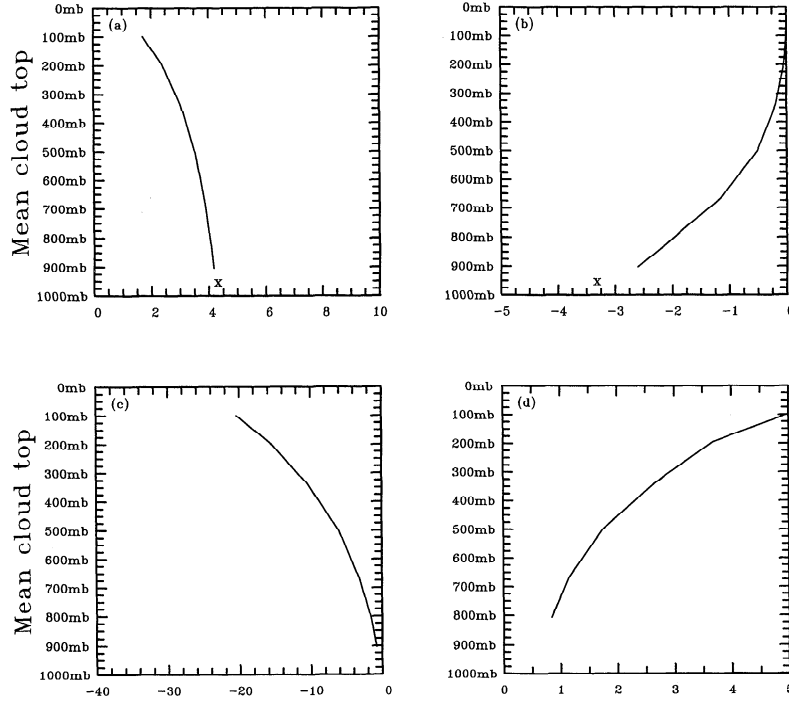
Figure 3. Dependence of various outgoing longwave radiation (OLR) contributions (Watts per square meter) as a function of mean cloud top for a cloudy region. (a) $(< G^n_T(0,\hat{p})T' >$ $+G^n_{T_s}(0)T'_s)$ for $T' = 1°K$ for all layers and $T'_s = 1°K$. (b) $< G^n_q(0,\hat{p})q' >$ for $q' = 1$ g/Kg for the layers 1000-667 mbar, $q' = 0.5$ g/Kg for 667-501 mbar, $q' = 0.1$ g/Kg for 501-336 mbar, $q' = 0.01$ g/Kg for 336-194 mbar, and $q' = 0.001$ g/Kg for 194-100 mbar. (c) $G_{\alpha_n}(0)\alpha'$ for $\alpha' = 10\%$ for the layers in which cloud exists. (d) $G_{p_{t_n}}(0)p'_t$ for $p'_t = 10$ mbar. In Figures 3a and 3b the value at 950 mbar ("x") represents clear sky.

emission occurs from a higher temperature for a lower cloud. This effect increases with height since the lapse rate (per millibar) is larger in the higher layers and there is less reabsorption.

4. Applications to the Annual Average Case

The analysis of the Green's functions in the last section suggests that the Green's functions are not sensitive over the tropics. Thus, we can use just one set of Green's functions corresponding to a typical reference profile in the tropics to model almost all of the tropical areas except for some very dry areas, such as the Sahara Desert, where some error will be incurred. In this section, the linearized scheme with one set of Green's functions is used to do a full test in comparing to the original scheme and the observations from CAC. The reference profile is a spatial average over the tropics (30N—30S) of the annual average climatology. The test region is confined within 30° latitude. Here, we focus on modeling the annual average response relative to the spatial mean; the seasonal cycle and an ENSO case will be discussed in the following section.

4.1. Clear Sky Case

Figures 4a–4b show the longwave radiative flux perturbation field from the nonlinear and the linearized
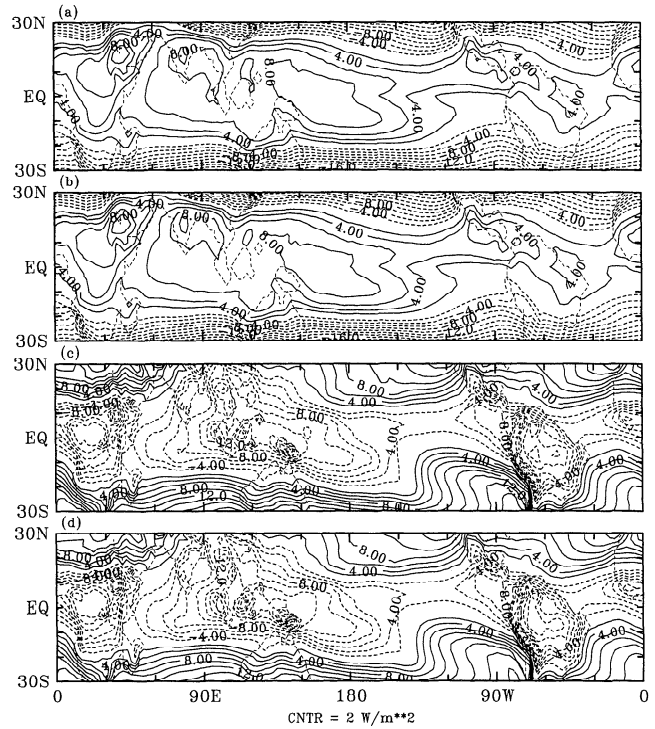

Figure 4. (a) OLR perturbations due to temperature departures from the spatial mean for the annual average clear sky case from the nonlinear scheme. (b) As in Figure 4a but from the linearized scheme. Figure 4c and 4d are same as Figure 4a and 4b, respectively, but for moisture variations.
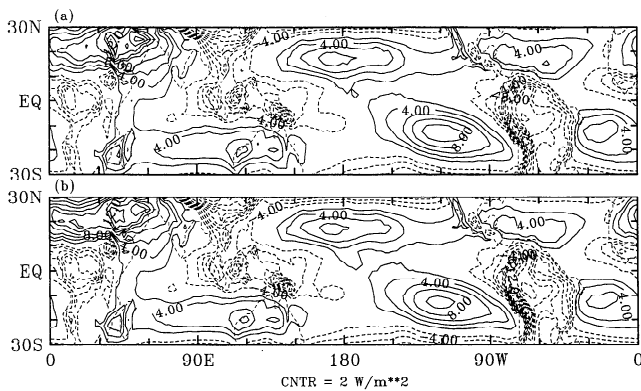
Figure 5. OLR perturbations due to combined temperature and moisture departure from the spatial mean for the annual average clear sky case (a) from the nonlinear scheme, and (b) from the linearized scheme.

schemes due to temperature departures from the spatial mean for clear skies. The linearized scheme mimics the nonlinear scheme to high accuracy. The OLR perturbation due to temperature variation is mainly contributed from the surface and lower atmosphere for a clear sky case, so the OLR perturbation is similar to the surface temperature pattern. The corresponding results for moisture departures from the spatial mean are given in Figure 4c-4d. Even though Figure 2b indicates some nonlinearity in the flux dependence on moisture, the linearized scheme still does a very good job of reproducing the nonlinear scheme.

Figures 5a-5b are the OLR perturbations in the clear sky from the nonlinear and the linearized schemes, respectively, when both temperature and moisture are included. For the linear case, Figure 5b is the sum of Figure 4b and Figure 4d. As in Figure 4, the linear scheme reproduces the nonlinear results extremely well, and the $T'q'$ nonlinearities included here do not change this agreement. The patterns due to temperature alone and moisture alone in Figure 4b and 4d tend to have similar patterns on the large scale, but with opposite signs. Regions of higher surface and tropospheric temperature tend to radiate more, while the greenhouse effect associated with greater moisture traps upgoing longwave radiation from the surface and lowest levels. When combined, there is considerable cancellation between these at the largest scales, leaving a smaller-scale pattern that accentuates the differences. These are associated with the greater extremes in the water vapor contribution, and largely associated with the elevated values in convergence zones and low values in a subtropical descent regions. Conventional Newtonian cooling, currently used in simple atmospheric models, would tend to resemble Figure 4b, and thus would fare poorly at representing the more complicated pattern of Figure 5. The fact that the water vapor greenhouse contribution overcomes the temperature contribution in convergence zones in Figure 5 is associated with controversy over what has been termed the "super-greenhouse effect " in these regions [*Ramanathan et al.*, 1995; *Pierrehumbert*, 1995]. The agreement with

the nonlinear model implies the linear scheme can be a useful tool for studies of this effect in intermediate atmospheric models. At higher latitudes in the subtropics, the OLR perturbation is negative as temperature effects become dominant, as expected.

4.2 Full Simulation: OLR

Figure 6 shows the OLR perturbations in the cloudy sky from the nonlinear scheme, two versions of the linearized scheme, the weakly nonlinear scheme and observations, respectively. Contributions from T', T_s', q' and α_n' are included in all cases (Figure 6a–6d). Since the nonlinear scheme does not have the contribution of the cloud top variation between two model layers, in order to compare the results of the linearized scheme directly to the nonlinear scheme, Figure 6b shows a case where the contribution of cloud top variation, p_{tn}', is excluded in the linearized scheme. As in the clear sky case, the linear scheme reproduces the nonlinear scheme with reasonable accuracy in Figure 6a and 6b. The cloud top effect contributes negative OLR perturbations in the deep convective region, bring-
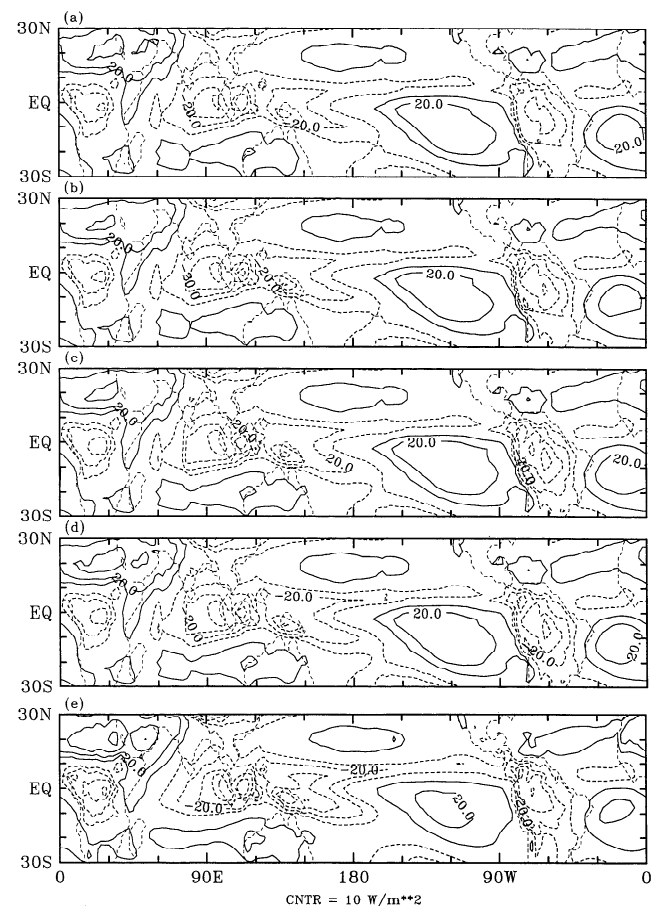

Figure 6. Annual average tropical climatology OLR as departure from the spatial mean from (a) the nonlinear scheme; (b) the linearized scheme without cloud top variations; (c) the linearized scheme including cloud top variation; (d) the weakly nonlinear scheme including cloud top variations; and (e) Climate Analysis Center (CAC) observations.

ing the total OLR perturbations from the linearized scheme shown in Figure 6c closer to the results of the CAC observations shown in Figure 6c. Of course, if much higher vertical resolution were used in the nonlinear scheme, it could also capture these cloud top variations, but with the GCM vertical grid used here, the linear scheme is actually more accurate. We should also note that comparison to observed OLR is essentially a consistency check, since we specify ISCCP cloud parameters that themselves have been derived from radiative transfer calculations. Figure 6d shows the results from the weakly nonlinear scheme, including p'_{tn} variations. The biggest differences from the linear scheme (linearized about a single reference profile and a set of cloud fraction values, α'_n) of Figure 6c are due to terms of the form $\alpha'_n q'$ in convective zones, and these reach only 2 W/m^2. Lesser contributions (that tend to be opposite sign) come from $\alpha'_n p'_{tn}$, while $\alpha'_n T'$ reaches only about 0.5 W/m^2. Overall, the differences are sufficiently small that the weakly nonlinear scheme offers only modest improvement. Some differences in spatial pattern may be noted in diagnostics, for instance, of q' contributions depending on whether the reference state includes spatial dependence of cloud fraction.

Figure 7 shows the contributions to the OLR perturbations of Figure 6c from temperature, moisture, cloud cover, and cloud top variations, respectively. Comparing to Figure 4, the contributions of temperature and moisture in the cloudy sky case are still close to the clear sky case: the spatial patterns are basically the
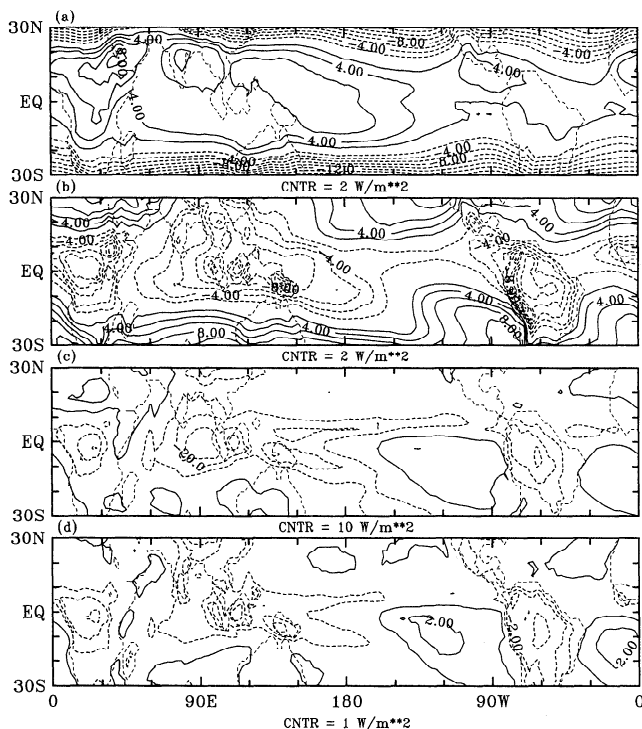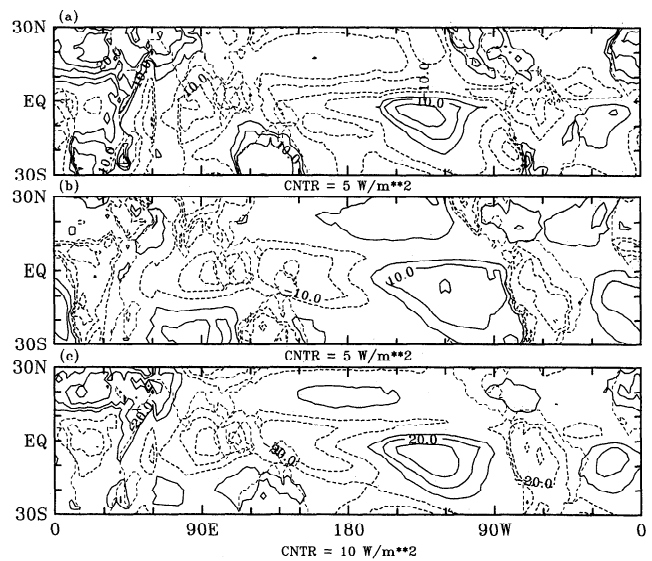

Figure 8. OLR calculated by the linear scheme as in Figures 6 and 7, but for a case that uses one cloud type only. (a) Contributions from cloud cover perturbations. (b) Contributions from cloud top perturbations. (c) Same as Figure 6c, but for one cloud type only.

same, although maxima are slightly reduced by the presence of clouds. The contribution of cloud cover variations (Figure 7c) has much larger local magnitudes than the other contributions, so this dominates the spatial pattern of OLR perturbations, resulting in a distribution very different from the clear sky case. However, the temperature and moisture effects have broader spatial scales and are physically important to balances integrated over large areas.

The spatial pattern of OLR clearly reflects the mean convective zones where larger high cloud fraction contributes negative OLR perturbations. In the cold tongue region, even though the perturbations of the low-cloud cover are strongly positive, negative perturbation of high-cloud cover leads to positive total OLR perturbation. *Ockert-Bell and Hartmann* [1992] have noted that high clouds have the strongest influence on OLR perturbations even in the areas which are covered by low clouds all the time, such as the cold tongue and midlatitude areas.

The contribution from the cloud top effect (Figure 7d) is not large in this three cloud-type case: part of the signal associated with cloud top changes is captured by changes in cloud type. With more cloud types (and high vertical resolution), explicit calculation of cloud top perturbations within each cloud type would become even less important. However, inclusion of the cloud top term does permit maintenance of relatively high accuracy with very few cloud types. Figure 8 shows results for a case that only has one cloud type, $\bar{p}_t = 501$ mbar. The linearized cloud top term is thus obliged to approximate all cloud top variations in the ISCCP data set. The OLR variations from cloud top changes have thus been partly shifted from the cloud cover effect to the explicit cloud top effect (see Figure 8a and 8b)

Figure 7. Contributions to the annual average OLR perturbations from the linearized scheme in Figure 6c from (a) temperature perturbations, (b) moisture perturbations, (c) cloud cover perturbations, and (d) cloud top perturbations.
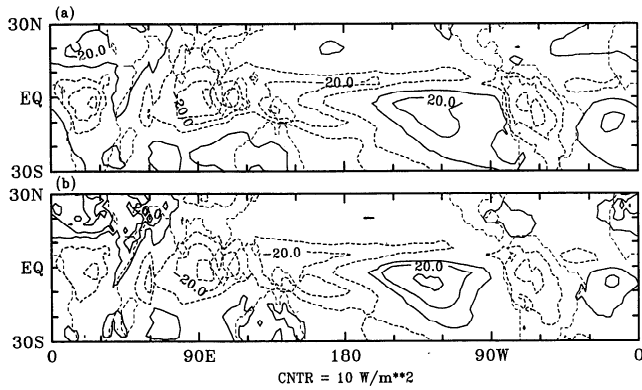
Figure 9. Total of cloud cover and cloud top contributions for (a) the three cloud type case (the sum of Figures 7c and 7d); (b) the one cloud type case (the sum of Figures 8a and 8b)

without changing the total cloud effect too much. The direct comparison of cloud contributions for three and one cloud-type cases in Figure 9 makes this clear. In other words, the linear effects of p'_t anomalies about mean cloud top for a single cloud type do an acceptable job of capturing many of the cloud effects. We note that the one cloud-type case has stronger magnitude in the areas with positive OLR perturbations and weaker magnitude in the negative areas, so the single cloud type case does have some error.

4.3 Full Simulation: Vertical Structure

Although we do not have observations for the vertical profile of fluxes and heating rate, we can still test the

performance of the linearized scheme by comparing with the nonlinear scheme. The results for an example on the equator at the dateline are shown in Figure 10. Perturbations from the tropical mean of heating rate and upward and downward fluxes from the nonlinear and linear schemes are very close: the curves that do not include the contribution of cloud top variation almost overlap. This is partly because errors in $R^\uparrow_{atm}$ and $R^\uparrow_{sfc}$ have opposite signs, and tend to cancel since the first is largely associated with emission and the latter with absorption. When cloud top variation is included in the linear scheme, it modifies the fluxes slightly and has some local impact on the heating rate perturbation near mean cloud top. In a discretized vertical coordinate, care must be taken in linearization of the downward flux to avoid creating unrealistic local heating rate in the layers below cloud top (see (8)).

Figure 11 shows heating rate profiles (as a departure from the space-time mean) in four selected regions: Figure 11a is in the cold tongue region, Figure 11b in the warm pool region, Figure 11c in the Sahara Desert, and Figure 11d in the Amazon rain forest. Here, the contribution of cloud top variation is omitted in the comparison. Overall, heating rate perturbations agree well between the nonlinear and the linearized schemes. The biggest differences occur in the lower layers, mainly due to effects of the second-order perturbation, $\alpha'_n q'$. This term strongly affects $R^\downarrow$ since the effects on $R^\uparrow_{atm}$ and $R^\uparrow_{sfc}$ cancel each other, so the simulations of OLR will be better than $R^\downarrow$. This effect does not appear in the clear sky case, so the error would be smaller than in
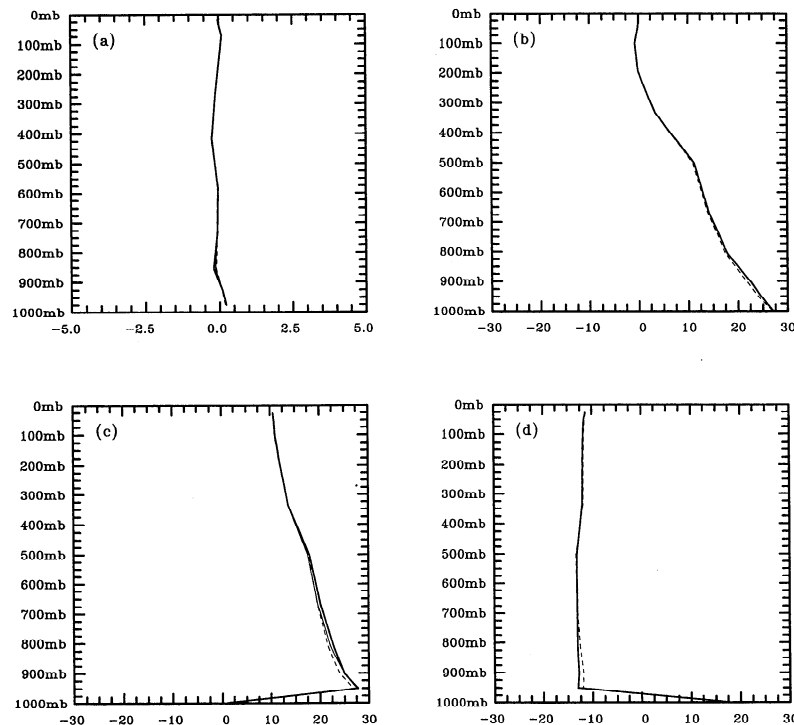

Figure 10. Vertical profiles (of departures from the space-time mean) from the nonlinear scheme (dashed line), the linearized scheme with fixed cloud top (thin solid line), and the linearized scheme (thick solid line) in a typical tropical region (at the dateline on the Equator): (a) heating rate (K d^{-1}), (b) $R^\downarrow$ (Wm^{-2}), (c) $R^\uparrow_{atm}$ (Wm^{-2}), and (d) $R^\uparrow_{sfc}$ (Wm^{-2}).
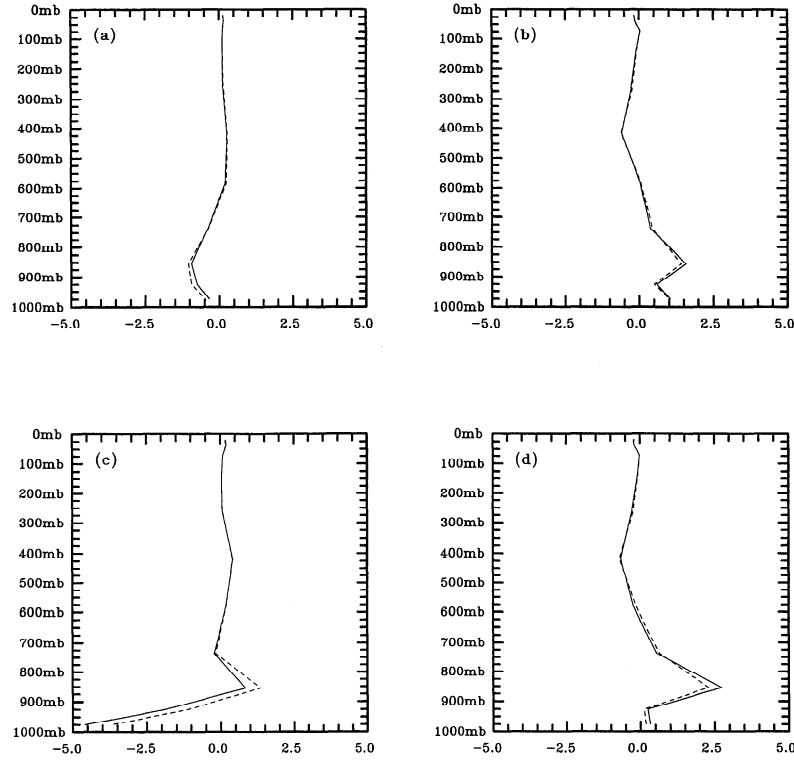
Figure 11. Vertical profiles of heating rate departures from the space-time mean (K d^{-1}) from the nonlinear scheme (dashed line) and the linearized scheme (solid line) in four typical regions: (a) cold tongue (at 120W and 10S), (b) warm pool (at 150 E and 5S), (c) the Sahara desert (at 30E and 20N), and (d) the Amazon (at 70W and the Equator).

the cloudy sky case. Note that we have linearized about a tropical average cloud amount, so the Sahara region incurs the worst error. If greater accuracy were desired there, additional clear sky Green's functions could be used. The weakly nonlinear scheme can marginally increase the accuracy (not shown). These examples span a variety of cloud effect cases: In Figure 11b, 11c, and 11d, the α'_n of low clouds are negative, so the heating rate perturbations of the lower layer are positive. In the cold tongue region (Figure 11a), the heating rate perturbation is negative because of positive α'_n of low cloud. In Figure 11b and 11d, which have large high cloud amounts, the upper level heating rate perturbations are negative. The linearized scheme tracks the nonlinear scheme quite well in representing these.

5. Applications to the Seasonal Cycle and an ENSO Case

5.1. The Seasonal Cycle

Figures 12, 13, and 14 show the seasonal cycle of OLR from the nonlinear version of the radiation scheme, the linear version, and the CAC data, respectively. The main features of the seasonal cycle in these three figures are almost the same, again indicating the fidelity of the linear scheme. The spatial patterns are dominated by the seasonal migration of the convergence zones, with negative anomalies in regions with greater convection than the annual average. Strong signals are formed over

land areas, such as the Amazon and western Africa, as the convergence zones move between the hemispheres; the Austro-Asian monsoon region exhibits a more complex pattern associated with monsoon onsets. Asym-
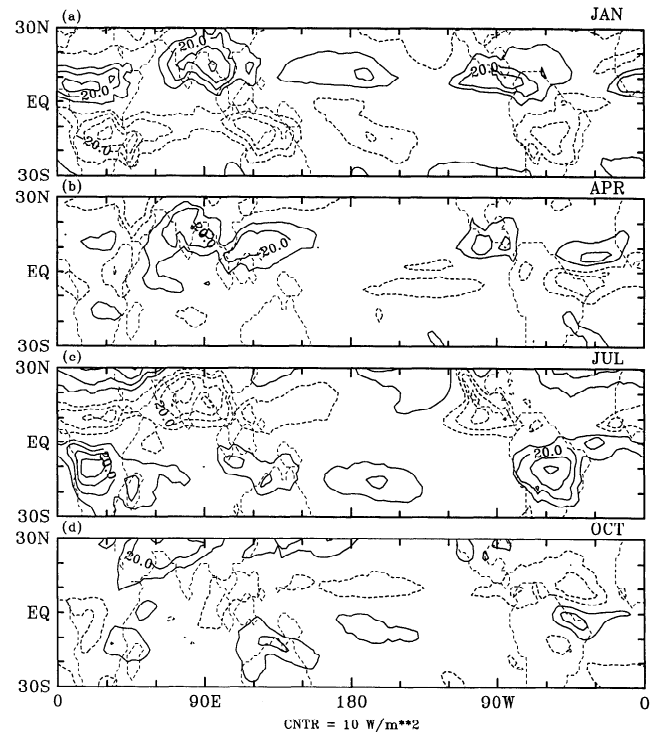

Figure 12. The seasonal cycle of OLR perturbations from the nonlinear scheme.
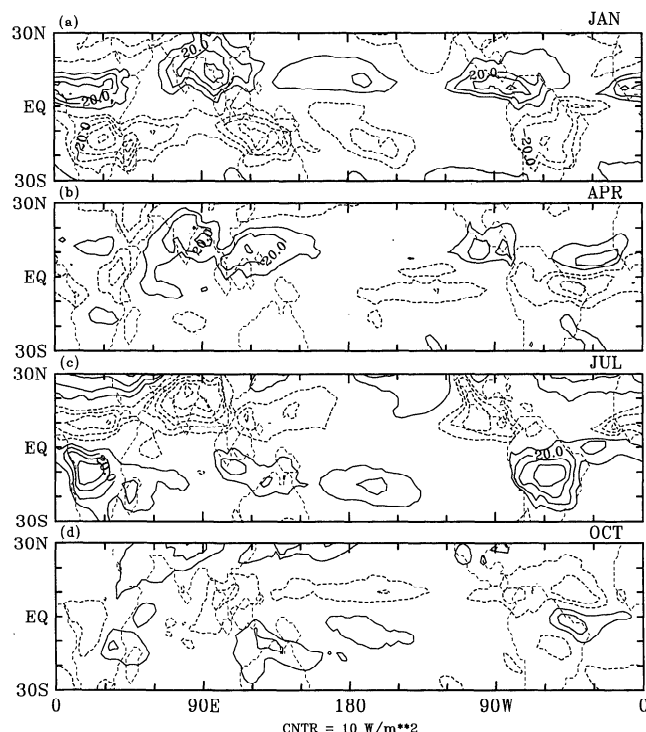
Figure 13. The seasonal cycle of OLR perturbations from the linearized scheme.

metry between winter and summer seasons and between the equinoxes may also be noted. Since the linearized longwave radiation scheme includes the contributions from the cloud top variations, its response (Figure 13) is closer to the observations (Figure 14) than the 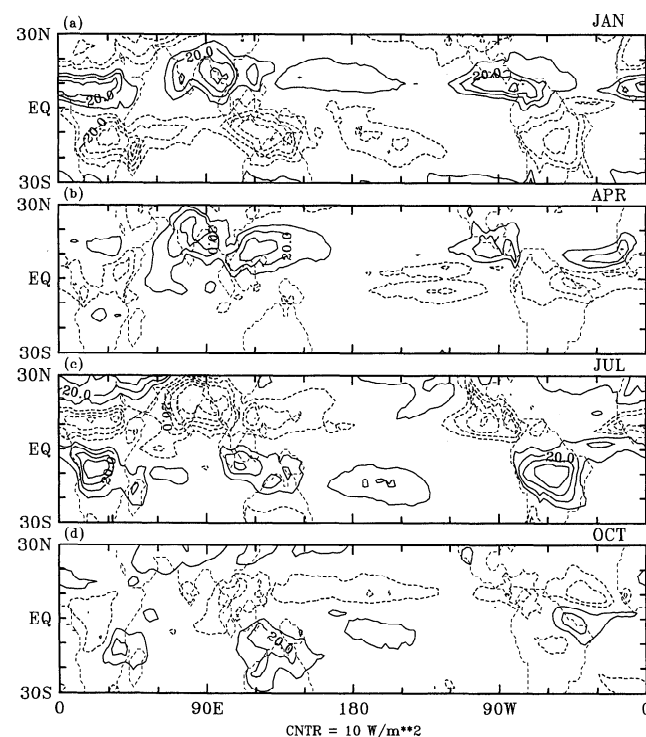nonlinear scheme (Figure 12). This was noted in the annual case, but in the seasonal cycle case, the difference is relatively larger, emphasizing the importance of cloud top variation. As in the annual case, the linear scheme is sufficiently accurate that improvements from the weakly nonlinear scheme are marginal.

Figure 15 shows the seasonal cycle for OLR spatially averaged over the entire tropical region from 30N to 30S. This provides an example of what happens at the largest spatial scales. In Figure 15a, the linear scheme reproduces the nonlinear scheme, as expected. There is some difference between the model results for the given data and observed OLR. This may be partly due to the interpolations of land surface temperature, but errors in, for instance, ECMWF moisture fields might contribute. The main point of this figure is that the contribution of cloud fraction (Figure 15c) is no longer the dominant term, and the contributions of temperature and moisture (Figure 15b) are equal magnitude. This differs substantially from the relative importance at spatial scales comparable to the convergence zones (e.g., Figure 7 or Figure 13), where cloud effects dominate. Because temperature and moisture effects occur at broader scales, they are as important as cloud longwave effects for the tropics as a whole. We note also that the relation between moisture and cloud effects at this large scale differs from what occurs at the scale of convergence zones, with cloud effects actually tending to have opposite sign.

5.2. The 1986–1987 ENSO

Since the ISCCP data covers July 1983 to June 1991, we use the 1986–1987 ENSO as an example of inter-

Figure 14. The seasonal cycle of OLR perturbations from CAC observations.
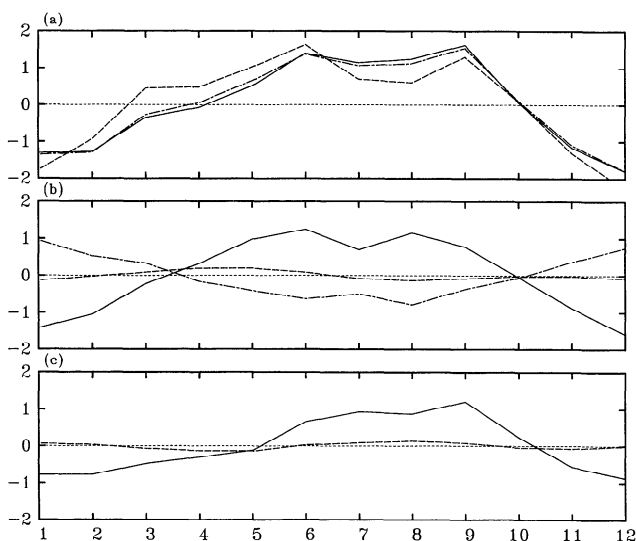

Figure 15. The OLR spatial mean over 30S–30N (Watts per square meter) for the seasonal cycle (as a departure from annual average). The abscissa is the month. (a) Total OLR from the nonlinear scheme (dot-dashed line), the linear scheme (solid line), and CAC observations (dashed line). (b) OLR contributions in the linear scheme from atmospheric temperature (solid line), surface temperature (dashed line), and moisture (dot-dashed line). (c) OLR contribution from cloud fraction (solid) and cloud top (dashed line).
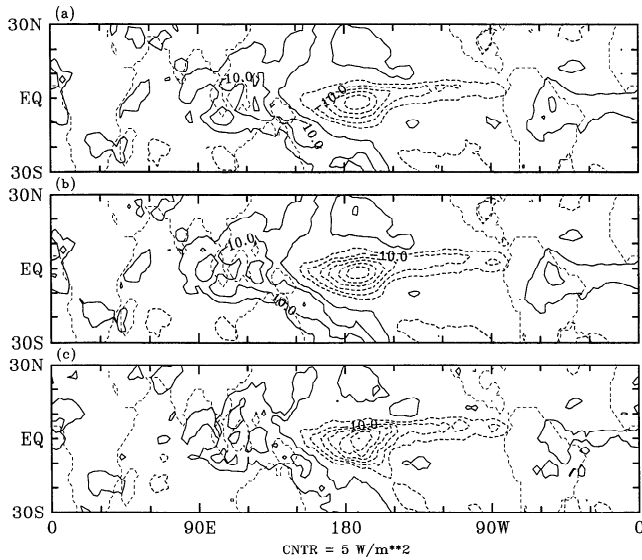
Figure 16. OLR anomalies during the 1986-1987 El Niño–Southern Oscillation (ENSO) warm phase averaged from December 1986 to November 1987 (a) from the nonlinear scheme, (b) from the linearized scheme, and (c) from CAC observations.

1994], and the model used to produce the ECMWF data has changed several times during the period we used to define the climatology. With these caveats in mind, we can nonetheless use the analysis fields to illustrate the use of the linearized scheme. Due to linearity, contributions to various variables can be additively separated, including, for instance, upper and lower tropospheric water vapor. Around the dateline at the equator (region 1), negative OLR anomalies are due to a positive moisture perturbation mainly in the upper troposphere (Figure 17d). The positive OLR anomaly around 150 W just south of the equator (region 2, Figure 17c and 17d) appears puzzling because low-level temperature is warm, and one might expect higher moisture to yield a negative contribution to
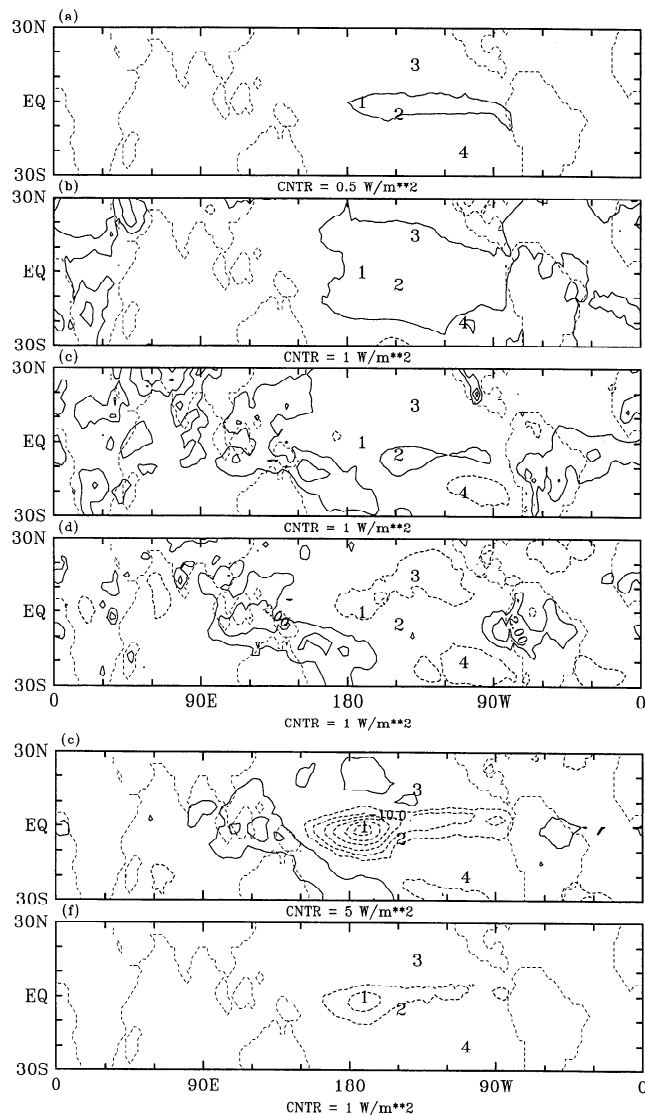
annual variability. To reduce noise associated with shorter timescale atmospheric variability, we averaged the data during the warm year, from December 1986 to November 1987. The nonlinear and linearized schemes each catch the main signal of ENSO, strong negative OLR perturbations are along the dateline (Figure 16). Comparing them more carefully, the results of the non-linear scheme are still a little weak compared to the observations. The magnitude of the ENSO signal in the linearized scheme that includes cloud top variation (the middle panel of Figure 16) lies between the observations and the nonlinear results. Once again, cloud top variation proves important to the OLR perturbation.

Figure 17 shows contributions to OLR due to T', T'_s, q', α' and p'_{tn}, respectively. The main contribution still comes from cloud cover variations (Figure 17e, 17f). These have a maximum near the dateline associated with convection, whose nonlocal relationship to SST anomalies has often been discussed [Gill and Rasmusson, 1983; Graham and Barnett, 1987; Lindzen and Nigam, 1987; Neelin and Held, 1987]. The contributions from temperature and moisture are small but broader. The SST anomalies are at the equator along the cold tongue, so the direct contribution of SST anomalies to OLR is limited to a narrow region (Figure 17a). However, the OLR anomalies from the atmospheric temperature anomalies are much wider (Figure 17b), since the latter are spread over characteristic atmospheric spatial scales on the order of the radius of deformation. Figure 17c and 17d show the OLR contribution due to ECMWF moisture anomalies in the lower atmosphere (below 500 mb) and in the upper atmosphere (above 500 mbar), respectively. The accuracy of moisture fields in the ECMWF analysis, especially at upper levels, is dubious [Salathé and Chesters, 1995; Al-Khalaf et al.,

Figure 17. The OLR perturbations of the 1986-1987 ENSO from the linearized scheme contributed by (a) surface temperature perturbations, (b) atmospheric temperature perturbations, (c) moisture perturbations below 500 mbar, (d) moisture perturbations above 500 mbar, (e) cloud cover perturbations, and (f) cloud top perturbations. The numbers indicate four regions discussed in text.
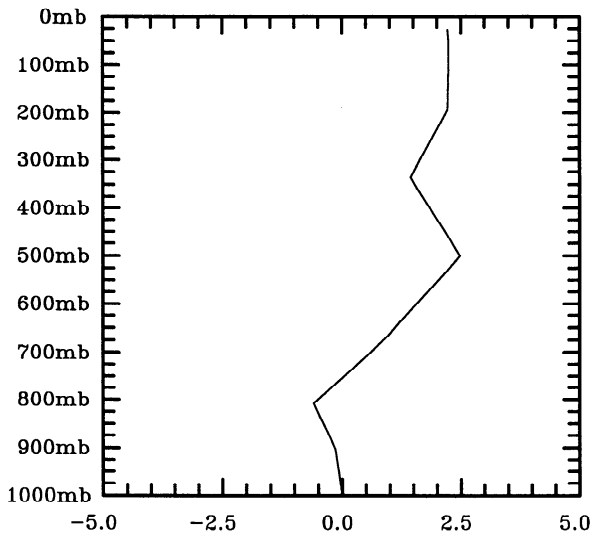
Figure 18. The vertical profile of the moisture contribution to upward longwave radiative flux (Watts per square meter) in region 2 (see Figure 17).

OLR anomalies. This indeed happens in the layer below 800 mbar, as may be seen in Figure 18 which shows the vertical profile of the moisture contribution to upward longwave radiative flux in this region. In the middle troposphere, decreased moisture due to subsidence reverses the contribution to OLR, in a manner roughly similar to the *Lindzen* [1990] hypothesis. On the other hand, the regions of negative OLR anomaly in the descent regions of the subtropical eastern Pacific (regions 3 and 4) are associated with increases in upper tropospheric moisture in the ECMWF data set. These are at odds with *Chou's* [1994] analysis based on clear column OLR (for April 1987 minus April 1885), and so we are inclined to doubt the accuracy of the ECMWF upper tropospheric moisture anomalies for these regions. While the problems in the ECMWF moisture fields preclude firm conclusions about moisture feedbacks in the real atmosphere, we note (1) that the linear radiation scheme accurately reproduces the nonlinear one for the given anomalies (2) that the linear diagnostics are useful for tracking behavior in analysis fields, such as the difference between proximal descent region 2 and distant descent regions 3 and 4 in the radiative effects of ECMWF moisture anomalies discussed above.

6. Conclusions

A Green's function technique is used to formulate and test a linear scheme for longwave radiative fluxes, based on a nonlinear radiative scheme used in GCMs. A weakly nonlinear version of the scheme is also tested. Longwave radiative flux perturbations due to vertical profiles of temperature and moisture perturbations, as well as cloud cover for multiple cloud types and cloud top perturbations can be calculated. Cloud cover types

are defined such that no vertical overlap occurs, so that linearization holds well for cloud fraction of each type. Linearization of cloud top dependence about mean cloud top for each cloud type is also included. This is of modest importance when three or more cloud types (as in the ISCCP data) are used but becomes very significant for simpler cases where one uses a single cloud type. The cloud type definitions used here are relatively simple but the scheme could accommodate more complex definitions. The Green's functions are defined by numerically linearizing the GCM nonlinear scheme and storing the small matrices associated with T and q, and the vectors associated with each cloud fraction and type. We use the Harshvardhan longwave radiative scheme here, although the method could be applied to other GCM schemes.

We test the linear scheme against the nonlinear Harshvardhan scheme in situations that might be encountered by intermediate atmospheric model simulations using ECMWF analysis fields for T and q and cloud cover and cloud top data prescribed from ISCCP observations. We use observations of OLR from CAC as a consistency check. We use Green's functions associated with linearization about a single typical profile for T, q, and cloud fractions and types (e.g., the tropical time and space mean). To our surprise, we find that the linear scheme reproduces the nonlinear results to very high accuracy, even for simulations of the tropical climatology (as a departure from its spatial average). For perturbations associated with the seasonal cycle and interannual variability, it does even better. This holds for vertical structures of the fluxes, aside from details associated with finite differencing. Both schemes do well at reproducing observed OLR when given cloud fraction and cloud top information. In fact, at typical GCM vertical resolutions, the linear scheme is slightly more accurate than the nonlinear scheme for OLR because of the explicit treatment of cloud top perturbations that are less than one grid interval in the vertical. For the simple cloud types used, downward fluxes might be less accurate compared to observations although we have not tested this. Maps of OLR contributions by various physical terms illustrate that the spatial variations contributed by cloud fraction and cloud top can be expected to be significant in simulation, for instance, of the tropical Walker circulation. Maxima and minima associated with temperature and moisture contributions are much smaller in magnitude, but the patterns tend to be of broader spatial extent so these become comparable to cloud contributions when averaged over large regions. We suggest all terms should be included in intermediate atmospheric models. Because the linear scheme does so well, the improvements offered by the weakly nonlinear version are modest, although they can be significant for downward fluxes at the surface where $\alpha' q'$ terms are noticeable.

The Green's function scheme thus appears highly suited for use in certain tropical modeling applications. Advantages that make the linearized scheme a use-

ful adjunct to the original include: (1) the linearized scheme is computationally very economical, and radiative computations are very time consuming in GCMs. In this linearized scheme, the integrations over spectral bands and interaction paths are done off-line, when the Green's functions are first computed. During model time integration, only (small) matrix multiplications with the Green's functions are required to obtain the radiative fluxes or heating. The linearized scheme is almost 25 times faster than the nonlinear *Harshvardhan et al.* [1987] scheme, which is one of the computationally more efficient schemes. The weakly nonlinear scheme is about 15 times faster (these factors are based on scalar computations on workstations; any vectorization or parallelization should be at least as favorable for the linear scheme as for the nonlinear scheme). If a more complex longwave radiative scheme were linearized, the speed up factor would be correspondingly greater. (2) The linear scheme permits additive decomposition of terms associated with different physical effects, which can aid diagnostics. (3) The principal advantage is that the linearized scheme can be used to make tropical theoretical and intermediate models more quantitative because it reproduces all essential features of a two-stream radiation scheme accurately in a form that is easy to apply. Most simple and intermediate atmospheric models currently used for studying ocean-atmosphere interaction have a simple form of Newtonian cooling for longwave radiation, depending only on temperature. The linearized scheme is almost as easy to use but correctly represents properties, such as transfer among atmospheric layers according to their absorptivity, and dependence on moisture. Unlike Newtonian cooling, the linear scheme distinguishes between longwave energy lost to space or transferred to another atmospheric layer, or the surface. This is crucial to coupling problems where surface heat balances are important, such as land surfaces or ocean regions not dominated by dynamical transports. As long as variations of temperature and moisture are known, this scheme can be easily used in any atmospheric model. If the models also calculate variations of cloud cover and cloud top, the linearized scheme will produce good quantitative simulation of the main longwave effects. In the near future, we expect this scheme will be applied in intermediate tropical atmospheric models.

Appendix A: Discretized Version of the Linearized Longwave Radiation Scheme

In section 2, the scheme was discussed in a vertically continuous notation. In practice, for vertical discretization by levels, the Green's functions become matrices of coefficients calculated from the original nonlinear scheme and stored as prescribed data for the linearized scheme. The scheme is restated here in matrix notation as an aid to users. The weakly nonlinear version (1) becomes:

$$
\underline{R} = \bar{\underline{R}} + \sum_{n=0}^{N} \alpha_n \underline{\underline{G}}_T^n \underline{T}'
$$
$$
+ \sum_{n=0}^{N} \alpha_n \underline{\underline{G}}_q^n \underline{q}'
$$
$$
+ \sum_{n=1}^{N} \underline{G}_{\alpha n} \alpha_n'
$$
$$
+ \sum_{n=1}^{N} \alpha_n \underline{G}_{p_{t_n}} p_{t_n}'
$$
$$
+ \sum_{n=0}^{N} \alpha_n \underline{G}_{T_s}^n T_s'. \tag{A1}
$$

The Green's functions for T, q and T_s are as in (2) but with p replaced by level index i and $\dot{p}$ replaced by j: $G_X^n(i,j) = \partial R(i)/\partial X(j)$. Green's functions for cloud fraction and top are as in (7) and (8).

As in Harshvardhan, a staggered grid is used with fluxes at half levels, and temperature and moisture at full levels (referred to as "layers"). If there are K layers in the model, then there are $K + 1$ flux values. Thus $\underline{\underline{G}}_T^n$ and $\underline{\underline{G}}_q^n$ are $(K + 1) \times K$ matrices. The effect of T_s is treated separately in $\underline{G}_{T_s}^n$, which is a vector with $K + 1$ components as are $\underline{G}_{\alpha_n}$ and $\underline{G}_{p_{t_n}}$.

The Green's functions are calculated numerically by putting a small perturbation at each layer for T and q and calculating the flux response per unit perturbation from the nonlinear scheme, and then verifying independence from size and sign of the perturbation. The nonlinear longwave radiation scheme is essentially treated as a black box so other longwave radiation schemes can be processed the same way.

In practice, the minimum longwave variables needed for coupled modeling are $Q_{LW}'(p)$ and $R^{Net}(p_s)$. For diagnostic purposes, it is convenient to have $R^\uparrow(p_s)$, $R^\downarrow(p_s)$, and $R^\uparrow(p_0)$ (i.e., OLR). We, therefore, offer a code version that uses a form close to the alternate formulation (5) but with the heating augmented by these three flux variables, given here for the weakly nonlinear version:

$$
\begin{bmatrix} Q_{LW}'(1) \\ \vdots \\ Q_{LW}'(K) \\ R^\uparrow(p_s) \\ R^\downarrow(p_s) \\ R^\uparrow(p_0) \end{bmatrix} = \sum_{n=0}^{N} \alpha_n \underline{\underline{H}}_T^n \underline{T}' + \sum_{n=0}^{N} \alpha_n \underline{\underline{H}}_q^n \underline{q}'
$$
$$
+ \sum_{n=1}^{N} \underline{H}_{\alpha n} \alpha_n' + \sum_{n=1}^{N} \alpha_n \underline{H}_{p_{t_n}} p_{t_n}'
$$
$$
+ \sum_{n=0}^{N} \alpha_n \underline{H}_{T_s}^n T_s', \tag{A2}
$$

where $\underline{\underline{H}}_T^n$ and $\underline{\underline{H}}_q^n$ are now $(K+3) \times K$ matrices which

are the $K \times K$ matrices for the heating corresponding to the continuous form (6), augmented by three rows for the top and bottom flux components, and so on.

The code for deriving and running the various versions of the linear and weakly nonlinear model is available from the authors. Currently, it may be accessed via the UCLA Department of Atmospheric Sciences Web Page: http://www.atmos.ucla.edu. We provide the code for the numerical linearizer, so that users may substitute their own longwave scheme, or choice of levels, etc., in deriving Green's functions. This code is provided without implied warranty.

Appendix B: Harshvardhan Longwave Radiation Scheme and Modifications

The Harshvardhan [*Harshvardhan et al.*, 1984, 1987] longwave radiation scheme is a two-stream radiative scheme without scattering or reflection. To reduce computational costs relative to the spectral "line-by-line" integration [*Stephens*, 1984], the method of *Chou* [1984], *Chou and Peng* [1983], and *Rodgers* [1968] is used to calculate the effects of water vapor, carbon dioxide and ozone based on the one-parameter scaling of *Chou and Arking* [1980]. Accuracy is discussed by *Chou et al.* [1991], and *Chou and Suarez* [1994] for the middle atmosphere.

The Harshvardhan scheme considers water vapor, carbon dioxide and ozone, omitting other absorbers, such as methane and aerosols. "E-type" absorption by water vapor is included, which strongly affects radiative cooling in the lower atmosphere, especially in high water vapor areas like the tropics [*Harshvardhan et al.*, 1989]. The Harshvardhan code allows cloud cover with fractional distribution from 0 to 1 and two kinds of cloud overlap, random and maximum, while in the vertical direction, clouds fill in a whole vertical model layer. Our cloud type treatment varies from this (see section 2). Clouds are treated as black bodies except for thin cirrus clouds and random cloud overlap in the Harshvardhan scheme. For the Green's function calculation here, we take all clouds to be black.

In our use of the scheme, the concentration of carbon dioxide is fixed at 330 parts per million by volume (ppmv), and the concentration of ozone is prescribed as a function of pressure typical of tropical climatology. A small modification to the numerical implementation was made in the formula used to fit scaled water vapor amount such that transmittance cannot become negative at high water vapor amounts. A cautionary note: ideally, any GCM code can be used as a black box for numerical linearization. In practice, we found that the interpolation used in certain tables in the code version inherited from the Colorado State University (CSU) GCM did not preserve continuity of functions and a modification back toward *Harshvardhan's* [1987] original formulation was necessary to ensure that first derivatives were well defined and continuous.

References

Al-Khalaf, A. K., D. T. Conlee, and T. T. Wilheit, Retrieval of atmospheric water vapor profiles from SSM/T-2 microwave radiances, Preprints, *Seventh Conference on Satellite Meteorology and Oceanography*, Monterey, CA Amer. Meteor. Soc., 106-109, 1994.

Cess, R. D., and G. L. Potter, Exploratory studies of cloud radiative forcing with a general circulation model, *Tellus*, *39A*, 460-473, 1987.

Chou, M. D., Broadband water vapor transmission functions for atmospheric IR flux computations, *J. Atmos. Sci.*, *41*, 1775-1778, 1984

Chou, M. D., 1994: Coolness in the tropical Pacific during an El Niño episode, *J. Clim.*, *7*, 1684-1692, 1994.

Chou, M. D., and A. Arking, Computation of infrared cooling rates in the water vapor bands, *J. Atmos. Sci.*, *37*, 855-867, 1980.

Chou, M. D., and L. Peng, A parameterization of the absorption in the 15 μm CO_2 spectral region with application to climate sensitivity studies, *J. Atmos. Sci.*, *40*, 2183-2192, 1983.

Chou, M. D., and M. J. Suarez, An efficient thermal infrared radiation parameterization for use in general circulation models, *NASA Tech. Memo*, *104606*, *3*, 1994.

Chou, M. D., D. P. Kratz, and W. Ridgway, Infrared radiation parameterizations in numerical climate models, *J. Clim.*, *4*, 424-437, 1991.

Curtis, A. R., 1956: The computation of radiative heating rates in the atmosphere, *Proc. R. Soc. London Ser. A*, *236*, 156-159, 1956.

Fels, S. B., and M. D. Schwarzkopf, An efficient, accurate algorithm for calculating CO_2 15 μm band cooling rates, *J. Geophys. Res.*, *86*, 1205-1232, 1981.

Gill, A. E., Some simple solutions for heat-induced tropical circulation, *Q. J. R. Meteorol. Soc.*, *106*, 447-462, 1980.

Gill, A. E., and E. M. Rasmusson, The 1982-1983 climate anomaly in the equatorial Pacific, *Nature*, *306*, 229-234, 1983.

Goody, R. M., and Y. L. Yung, *Atmospheric Radiation Theoretical Basis*, 2nd ed., Oxford Univ. Press, New York, 1989.

Graham, N. E., and T. P. Barnett, Sea surface temperature, surface wind divergence, and convection over tropical oceans, *Science*, *238*, 657-659, 1987.

Harshvardhan, and T. G. Corsetti, Longwave radiation parameterization for the UCLA/GLAS GCM, *NASA Tech. Memo. 86072*, 51, 1984.

Harshvardhan, R. Davies, D. A. Randall, and T. G. Corsetti, A fast radiation parameterization for general circulation models, *J. Geophys. Res.*, *92*, 1009-1016, 1987.

Harshvardhan, D. A. Randall, T. G. Corsetti, and D. A. Dazlich, Earth radiation budget and cloudiness simulations with a general circulation model, *J. Atmos. Sci.*, *46*, 1922-1942, 1989.

Houghton, J. T., G. J. Jenkins, and J. J. Ephraums (Eds.), *Climate Change: The Intergovernmental Panel*

on Climate Change Scientific Assessment, 364 pp., Cambridge Univ. Press, New York, 1990.

Houze, R. A., Jr., Cloud clusters and large-scale vertical motions in the tropics, J. Meteorol. Soc. Jpn, 60, 396-409, 1982.

Kiehl, J. T., R. J. Wolski, B. P. Briegleb, and V. Ramanathan, Documentation of radiation and cloud routines in the NCAR Community Climate Model (CCM1), Rep. NCAR/TN-288+IA, 109 pp., Natl. Cent. Atmos. Res., Boulder, Colo., 1987.

Lacis, A. A., and V. Oinas, A description of the correlated k distribution method for modeling nongray gaseous absorption, thermal emission, and multiple scattering in vertically inhomogeneous atmospheres, J. Geophys. Res., 96, 9027-9064, 1991.

Lindzen, R. S., and S. Nigam, On the role of sea surface temperature gradients in forcing low-level winds and convergence in the tropics, J. Atmos. Sci., 44, 2418-2436, 1987.

Lindzen, R. S., Some coolness concerning global warming, Bull. Am. Meteorol. Sci., 71, 288-299, 1990.

Liou, K.N., Analytic two-stream and four-stream solutions for radiative transfer, J. Atmos. Sci., 31, 1473-1475, 1974.

Liou, K.N., An Introduction to Atmospheric Radiation, Academic, San Diego, Calif., 1980.

Morcrette, J.-J., Impact of changes to the radiation transfer parameterizations plus cloud optical properties in the ECMWF model. Mon. Weather Rev., 118, 847-873, 1990.

Nagai, T., T. Tokioka, M. Endoh, and Y. Kitamura, El Niño-Southern Oscillation simulated in an MRI atmosphere-ocean coupled general circulation model. J. Clim., 5, 1202-1233, 1992.

Neelin, J. D., A note on the interpretation of the Gill model. J. Atmos. Sci., 46, 2466-2468, 1989.

Neelin, J. D., and I. M. Held, Modeling tropical convergence based on the moist static energy budget. Mon. Weather Rev., 115, 3-12, 1987.

Ockert-Bell, M. E., and D. L. Hartmann, The effect of cloud type on earth's energy balance: Results for selected regions, J. Clim., 5, 1157-1171, 1992.

Pierrehumbert, R. T., Thermostats, radiator fins and the local runaway greenhouse, J. Atmos. Sci., 52, 1784-1806, 1995.

Ramanathan, V., The role of Earth radiation budget studies in climate and general circulation rerearch, J. Geophys. Res., 92, 4075-4095, 1987.

Ramanathan, V., and P. Downey, A nonisothermal emissivity and absorptivity formulation for water vapor, J. Geophys. Res., 91, 8649-8666, 1986.

Ramanathan, V., Hypotheses for regulation of maximum SST: Test by CEPEX and other field data. Proc. Symp. Regulation of Sea Surface Temp. and Warming of the Trop. Ocean Atmos. Sys., Dallas, TX, Am. Meteorol. Soc., Jan. 15-20, 1995, pp. 90-95, 1995.

Randall, D. A., Harshvardhan, D. A. Dazlich, and T. G. Corsetti, Interactions among radiation, convection, and large-scale dynamics in a general circulation model, J. Atmos. Sci., 46, 1943-1970, 1989.

Rodgers, C. D., Some extension and applications of the new random model for molecular band transmission, Q. J. R. Meteorol. Soc., 94, 99-102, 1968.

Rossow, W. B., and R. A. Schiffer, ISCCP cloud data products, Bull. Am. Meteorol. Sci., 72, 2-20, 1991.

Salathé, E. P., Jr., and D. Chesters, Variability of moisture in the upper troposphere as inferred from TOVS satellite observations and the ECMWF model analyses in 1989, J. Clim., 8, 120-132, 1995.

Seager, R., A simple model of the climatology and variability of the low-level wind field in the tropics, J. Clim., 4, 164-179, 1991.

Seager, R., and S. E. Zebiak, Simulation of tropical climate with a linear primitive equation model, J. Clim., , 8, 2497-2520, 1995.

Slingo, A., and M. Slingo, The response of a general circulation model to cloud longwave radiative forcing, I, Introduction and initial experiments, Q. J. R. Meteorol. Soc., 114, 1027-1062, 1988.

Stephens, G. L., The parameterization of radiation for numerical weather prediction and climate models, Mon. Weather Rev., 112, 826-867, 1984.

Wang, B., and T. Li, A simple tropical atmosphere model of relevance to short-term climate variations, J. Atmos. Sci., 50, 260-284, 1993.

Webster, P. J., 1981: Mechanisms determining the atmospheric response to sea surface temperature anomalies, J. Atmos. Sci., 38, 554-571, 1981.

Zebiak, S. E., Atmospheric convergence feedback in a simple model for El Niño, Mon. Weather Rev., 114, 1263-1271, 1986.

Zou, J. and I. M. Navon, The development and verification of the adjoint of radiation transfer Process in the NMC spectral model, 1, Solar Radiative Transfer, Meteorol. Atmos. Phys., 58, 193-203, 1996.

Chia Chou and J. David Neelin, Department of Atmospheric Sciences, University of California, Los Angeles, Los Angeles, CA 90095. (e-mail: chia@atmos.ucla.edu; neelin@atmos.ucla.edu)